RSC Advances

PAPER

View Article Online
View Journal | View Issue

Cite this: *RSC Adv.*, 2024, **14**, 32460

P-Sulfonatocalix[4]arene turns peptide aggregates into an efficient cell-penetrating peptide†

Mahsima Heydari,[a] Najmeh Salehi,[b] Reza Zadmard,[c] Werner M. Nau,[d] Khosro Khajeh,[e] Zahra Azizi[f] and Amir Norouzy*[a]

Received 21st September 2024
Accepted 8th October 2024

DOI: 10.1039/d4ra06124a

rsc.li/rsc-advances

A novel cell-penetrating peptide (CPP) called *FAM*-Y_4R_4, with *FAM* as a fluorescent probe, was developed. Initially, we aimed to use Y_4 as a supramolecular host for water-insoluble drugs, with R_4 driving the complex into cells. However, an unexpected hurdle was discovered; the peptide self-assembled into amorphous aggregates, rendering it ineffective for our intended purpose. Molecular dynamics simulations revealed that intermolecular cation–π interactions between arginine and tyrosine caused this aggregation. By decorating the R_4 sidechains with *p*-sulfonatocalix[4]arene (CX4), we successfully dissolved most of the aggregates, significantly improved the peptide's solubility and enhanced the cell uptake with MCF7 and A549 cells *via* both direct penetration and endocytosis. The binding strength between CX4 and R_4, as well as the interaction between curcumin and tyrosines was quantified. Encouragingly, our results showed that *FAM*-Y_4R_4, with CX4, effectively delivered curcumin – as a model for poorly water-soluble drugs – into cells which exhibited potent anticancer activity. Using R_4/CX4 instead of the conventional R_{7-9} oligoarginine-based CPP simplifies peptide synthesis and offers higher yields. CX4 shows promise for addressing aggregation issues in other peptides that undergo a similar aggregation mechanism.

Introduction

The poor solubility and cell membrane impermeability often limit the effectiveness of many therapeutic agents.[1] Although significant progress has been made in drug delivery, intracellular delivery of many drugs and therapeutic agents still remains a challenge.[2] Among the various drug carriers, cell-penetrating peptides (CPPs) are capable and effective carriers for the intracellular delivery of a variety of cargoes, such as small molecules, nucleic acids, viruses, imaging contrast agents, and nanoparticles.[3] CPPs are easily synthesized on a large scale and because of their low molecular weight do not trigger an immune response. Numerous CPP-conjugated drugs are making their way to the bedside for reducing inflammation and pain, cancer therapy, curing heart diseases, anti-aging medications and even for diagnostic purposes.[4]

Based on their physicochemical properties, CPPs are classified into three groups: cationic, hydrophobic and amphipathic. Amphipathic CPPs are composed of a hydrophobic part at one end and a hydrophilic part at the other end. Poorly water-soluble drugs (PWSDs) are hydrophobic molecules that often exhibit limited bioavailability. Using CPPs for increasing their solubility and bioavailability is therefore the goal of many research studies. Cationic CPPs frequently have the least affinity for the PWSDS. Hydrophobic CPPs on the other hand can bind to PWSDs but do not increase their solubility, whereas amphipathic CPPs can bind to PWSDs from their hydrophobic part and increase drug solubility with their hydrophilic part. The hydrophilic part is usually composed of cationic amino acids.

In this study, we designed *FAM*-Y_4R_4 (Fig. 1) as an amphipathic CPP to deliver curcumin to cells. Beside its therapeutic property curcumine served as a model for PWSD. *FAM* is the commercial name for 5-carboxyfluorescein –a fluorescent probe– that is extensively used for labeling peptides. *FAM*-Y_4 is the hydrophobic part designed for biding to curcumin. R_4 is both the hydrophilic and the cell-penetrating part. Arginine is the most effective amino acid for enhancing the cellular uptake of cationic or amphipathic CPPs.[5,6] The permeability of arginine residues can be attributed to the ability of their guanidine group to form hydrogen bonds with the negatively charged groups on the cell membrane, such as carboxylic acid, sulfate, and phosphate.[7]

Unfortunately, extensive intermolecular cation–π interactions between the sidechains of arginine and tyrosine residues led to aggregation. These aggregates were rendered useless as they

[a]*Bioprocess Engineering Department, National Institute of Genetic Engineering and Biotechnology (NIGEB), Tehran, Iran. E-mail: a.norouzy@nigeb.ac.ir*
[b]*School of Biology, College of Science, University of Tehran, Tehran, Iran*
[c]*Department of Organic Chemistry, Chemistry and Chemical Engineering Research Center of Iran, Tehran, Iran*
[d]*School of Science, Constructor University, Bremen, Germany*
[e]*Department of Biochemistry, Faculty of Biological Sciences, Tarbiat Modares University, Tehran, Iran*
[f]*Department of Molecular Medicine, School of Advanced Technologies in Medicine, Tehran University of Medical Sciences, Tehran, Iran*

† Electronic supplementary information (ESI) available. See DOI: https://doi.org/10.1039/d4ra06124a

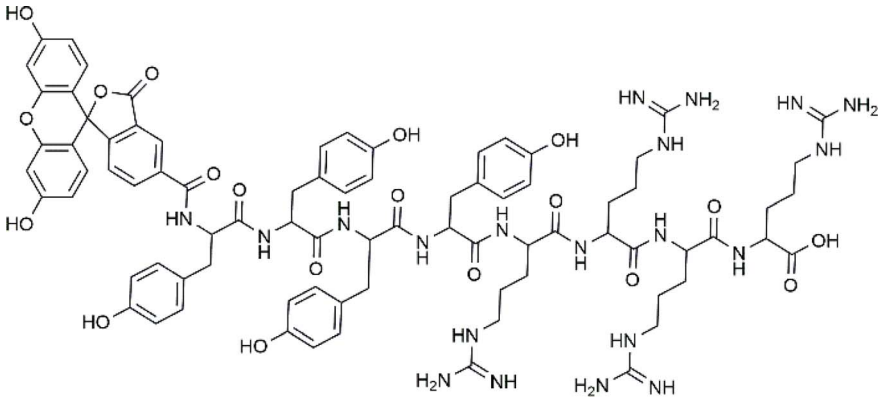

Fig. 1 Chemical structure of *FAM*-Y_4R_4 peptide, with FAM as a 5-carboxyfluorescein fluorescent dye attached to the N-terminus.

precipitated and did not enter the cells. Amphipathic peptides, in general, have a tendency to aggregate or to form micelles. Aggregation reduces the effective hydrophobicity of amphiphilic peptides by concealing their nonpolar parts from the surrounding aqueous environment.[8] Sometimes amphipathic peptides aggregated on the surface of the cells abolish their uptake.[9] Developing the strategies to inhibit amphipathic peptides from aggregation is therefore crucially important.[10] We successfully solubilized the majority of peptide aggregates by decorating the arginine side chains with *p*-sulfonatocalix[4]arenes (CX4). CX4 is a member of calixarene family. Calixarens are efficient molecular host for variety of cargos including peptides.[6,11,12] Decoration of the arginine sidechain with CX4 liberated the arginines from the tyrosines and drastically improved the solubility of the peptides. The solubilized peptide demonstrated promising cell uptake and cargo-carrying capabilities. This approach serves as a proof-of-principle for addressing similarly-aggregated peptides resulting from intramolecular cation–π interactions involving lysine or arginine side chains (as cation donors) and aromatic side chains of tryptophan, tyrosine, or phenylalanine (as π donors). It is worth noting that CX4 also binds to lysine side chains,[13] similar to arginine,[14] and is able to prevent its binding to the aromatic side chains.

Curcumin has been identified as the most important active ingredient in turmeric with a wide range of therapeutic benefits such as anti-cancer, anti-oxidant, anti-inflammatory, anti-thrombotic, and anti-microbial effects.[15] However, its usage is limited due to its poor aqueous solubility, low bioavailability, and rapid metabolism. The aim of using a CPP is to increase the solubility of curcumin and translocate it across the cell membrane. Due to its pharmaceutical importance and its aromatic structure, to bind to Y_4, we chose curcumin as a PWSD model to be carried with our peptide into the cells.

Materials and methods

Peptide preparation

FAM-Y_4R_4 was synthesized with the solid-phase peptide synthesis (SPPS) method using the Fmoc strategy.[16–18] We used 2-chlorotrityl chloride (CTC) resin as the solid phase. The synthesized peptide was cleaved from the resin using a cleavage cocktail containing 90% trifluoroacetic acid, 5% phenol, 2.5% water, and 2.5% triisopropylsilane as a scavenger. The crude peptide was precipitated using cold diethyl ether and subsequently dissolved in a solution consisting of 50% acetonitrile in water. The crude peptide was purified with a reversed-phased semi-preparative HPLC instrument equipped with a C_{18} column (21.2 × 150 mm, 5 μm). The purity of the peptide was assayed by an analytical HPLC instrument. The accuracy of the synthesis was confirmed by mass spectrometry. See the ESI† for details of the synthesis, purification, and mass spectroscopy.

Dynamic light scattering (DLS)

FAM-Y_4R_4 solutions were prepared at a concentration of 8 μM in 10 mM phosphate buffer with a pH of 7. Both solutions with and without 4 millimolar CX4 were prepared. The particle diameter was measured using a NanoBrook Omni instrument from Malvern, which was equipped with a 4 mW He/Ne laser at a wavelength of 633 nm. The measurements were taken at a fixed detector angle of 173°, utilizing an avalanche photodiode detector.

Field emission scanning electron microscopy (FE-SEM)

Peptide solution by the concentration of 50 μM were prepared in the phosphate buffer. For dissolving the peptide aggregates, CX4 was added to the peptide and the mixture was sonicated for 15 min followed by stirring at room temperature for an hour. The FE-SEM images were obtained using a MIRA3 TESCAN-XMU electron microscope at a voltage of 15 kV. The mean particle diameters of the images were calculated using ImageJ.

Molecular dynamics (MD) simulation of the peptide aggregation

The 3D structure of the *FAM*-Y_4R_4 peptide was modeled. Three of 50 ns MD simulations were performed for 150 ns to sample different conformations of *FAM*-Y_4R_4. The four most stable monomer conformations of *FAM*-Y_4R_4 were extracted using clustering analysis on the MD simulations trajectory of the *FAM*-Y_4R_4 monomer. These four peptide conformations were randomly placed in the two different simulation boxes with at least a 6 Å distance between them. In each system, after

equilibration, the production run was carried out for 100 ns. All MD simulation parameters and structural analysis were explained in the ESI.†

Cellular uptake

MCF-7 and A549 cells were purchased from the Iranian Biological Resource Center. The cells were grown in DMEM/F12 culture medium containing 10% heat-inactivated fetal bovine serum (FBS) and 1% of penicillin/streptomycin in a humidified incubator with 5% CO_2 and temperature fixed to 37 °C. Cellular uptake of the peptide and peptide/CX4 complex was confirmed using flow cytometry, fluorescence microscopy, and confocal laser scanning microscopy (CLSM).

Flow cytometry. The cells were seeded at a density of 1×10^5 cells per well in 24-well plates and treated with varying concentrations of the peptide and peptide/CX4 complex (ranging from 100–1200 nM) for 1 or 18 hours in the incubator. Afterward, the cells were washed three times with PBS, trypsinized, and spun down. The cell pellets were resuspended in 800 μL of PBS, and their fluorescence intensities were measured using a flow cytometer. The data obtained were analyzed using FlowJo software, and the mean fluorescence intensity (MFI) of live cells was determined.

Fluorescent microscopy. The cells were seeded at a density of 1×10^4 cells per well in 96-well plates and incubated with *FAM*-Y_4R_4 or *FAM*-Y_4R_4/CX4 for 18 h. Then the medium was removed and the cells were washed three times with PBS. Finally, Tyrod's solution was added to the wells and the images were taken by a fluorescent microscope.

Confocal laser scanning microscopy (CLSM). The cells were seeded at a density of 1×10^5 cells per well in 24-well plates with coverslips and incubated with *FAM*-Y_4R_4 (50 μM) or *FAM*-Y_4R_4/CX4 (50 μM/1 mM) for a duration of 18 hours. To stain the nucleus, the cells were also treated with 6,4-diamidino-2-phenyl indole (DAPI) dye (5 μg mL^{-1}) for 10 minutes. Subsequently, the cells were washed with PBS, and fixed on coverslips using paraformaldehyde (4%). The coverslips were mounted and the images were captured using a Leica TCS SPE confocal microscope which excited *FAM* with its 488 nm laser beam. The pinhole was adjusted to capture images of the middle section of the cells with the thickness of one Airy unit.

Measuring the binding constants

The binding constants (K_a) of the arginine sidechains to CX4 and the K_a of curcumin to tyrosine and phenol (as representatives of the binding domain, Y_4) were determined using the following methods.

Fluorescence titration. Tyrosine was fluorescently titrated with curcumin. The fluorescence spectra were acquired by exciting tyrosine at 280 nm and recording the fluorescence intensities from 290 to 390 nm. The binding isotherm was generated by plotting the fluorescence intensity at λ_{max} = 330 nm against the concentration of curcumin. The K_a values were subsequently calculated from the plot using OriginLab software, which employed a non-linear regression algorithm for the calculation.

UV-vis titration. To further confirm the π-stacking interaction between curcumin and the tyrosine sidechain, the binding constant of curcumin to phenol (serving as a representative of the tyrosine sidechain) was measured. Curcumin was spectroscopically titrated with phenol using an Analytik Jena Specord S100 spectrophotometer. The binding isotherm was plotted at $\lambda_{max} = 430$ nm, and the binding constant was calculated using OriginLab software and the non-linear regression algorithm described above.

Indicator displacement assay (IDA). To address the lack of spectral signal for calculating the K_a of the arginine sidechains to CX4, we employed the IDA method. In this approach, CX4 molecules were primarily loaded with the lucigenin (LCG) fluorophore. This resulted in the formation of the CX4/LCG complex, where the fluorescence of LCG was quenched. Subsequently, we incubated CX4/LCG with *FAM*-Y_4R_4, causing the arginine sidechains to replace LCG. The liberated LCG exhibited a fluorescence turn-on effect, which was utilized to plot the binding isotherm of the arginine sidechains to CX4.[19] Finally, the K_a value was calculated from the binding isotherm plot. Further details regarding this method can be found in the ESI.†

In vitro cytotoxicity study

The viability of MCF-7 and A549 cells were assessed in the presence of peptide, curcumin, peptide/curcumin, peptide/CX4, peptide/CX4/curcumin or CX4 using the colorimetric 3-(4,5-dimethylthiazol-2-yl)-2,5-diphenyltetrazolium bromide (MTT) assay. The cells were seeded at a density of 1×10^4 cells per well in a 96-well plate and treated with different concentrations of the aforementioned samples in triplicates for 18 h. The cell's viability was assayed with the MTT stablished protocol. The absorption of the treated and untreated cells at 570 nm was measured using the BioTek Epoch2 microplate spectrophotometer. The results are presented as mean ± standard error. The Tukey test was employed to determine the statistical significance with P-values < 0.05.

Results and discussion

Peptide design, synthesis and purification

We have designed *FAM*-Y_4R_4 which is composed of three parts: tetraarginine as the cell-penetrating part, tetratyrosine as the binding site and *FAM* as the fluorescence label (Fig. 1). As a result, this peptide is capable of: (i) entering the cells by its tetraarginine part (ii) binding to hydrophobic cargos *via* its tetratyrosine part and (iii) is fluorescently traceable inside live cells. The *FAM* molecule, being hydrophobic, is intentionally attached to the Y_4 part to ensure that all hydrophobic groups are located on one side, away from the R_4. This arrangement makes *FAM*-Y_4R_4 amphipathic. The amphipathicity allows the peptide to bind to hydrophobic cargos and simultaneously increase the solubility of the cargo.

In the pursuit of finding shorter peptides capable of cell penetration, researchers have explored truncated versions of Tat_{37-72}. Vivès *et al.* identified a positively charged, 13 amino acid domain (Tat_{48-60}) responsible for cellular uptake.[20]

Subsequent research by Park *et al.* further truncated it to Tat_{49-57} without significant loss of penetration capability.[21] In our study, we opted for a shorter oligoarginine sequence instead of the traditional R_7–R_{15} due to synthetic concerns, such as low yield associated with longer homorepeat of arginine. Adding even a single arginine to any peptide sequence proved challenging during peptide synthesis. On the other hand, CPPs shorter than eight amino acids, particularly oligoarginine peptides with fewer than eight arginine residues, exhibit poor cellular uptake.[22] To address this issue, we compensated for the poor cellular uptake of R_4 by attaching it to CX4. The preparation of R_4/*n*CX4 is easier and more cost-effective compared to synthesizing R_8. As a result, *FAM*-Y_4R_4 was synthesized with a high yield, and the peptide purity is approximately 99% while it exhibited promising cell uptake. The accuracy of the synthesis was confirmed by the mass spectrum (Fig. S1†).

Peptide self assembly

The peptide underwent self-assembly, forming nanostructural aggregates as observed through DLS and FE-SEM imaging (Fig. 2).

The predominant particle sizes, as determined by DLS, were approximately 3726 nm and 228 nm. We conducted circular dichroism (CD) spectroscopy on *FAM*-Y_4R_4 in order to identify α-helix or β-sheet structures. However, the CD spectrum did not exhibit any characteristics of these secondary structures (Fig. S2†).[23] Upon adding CX4 to the peptide solution, some of the aggregates completely dissolved, while the remaining aggregates shrank into nanoparticles with a mean size ranging from 74 to 180 nm. FE-SEM images were taken before and after the addition of CX4 to visualize the peptide aggregates. The average diameter of the aggregates in the images was measured to be 142 ± 19.1 nm. Following the addition of CX4, the mean size of the aggregates in the images decreased to 42 ± 8.7 nm. To explain this observation, we hypothesized that there was a cation–π interaction between the sidechains of arginines and tyrosines. Because when the guanidino group of the arginine sidechains entered the CX4 cavity it became inaccessible for interaction with the tyrosine sidechains, resulted in dissolving the aggregates (Fig. 2A).[19] To illustrate the cation–π interaction, we performed a spectral titration of phenol, representing the tyrosine side chain, with guanidine HCl, as the side chain of arginine. The spectral titration yielded a binding isotherm, from which a K_a value of $9.7 \times 10^5\ M^{-1}$ and the binding energy of 8.13 kcal mol^{-1} was calculated (Fig. S3†). In general, smaller cations exhibit stronger interactions with π systems. For instance, the binding energies of Li^+ and NH_4^+ to benzene are 38 and 19 kcal mol^{-1} respectively.[24] Since guanidino is larger than these ions, its binding energy is comparatively lower. Numerous studies have extensively reported the presence of cation–π interactions within protein structures, wherein the side chains of lysine or arginine interact with the side chains of phenylalanine, tyrosine, or tryptophan residues governing important biological processes.[24]

To gain further insights into the aggregation mechanism, we conducted MD simulations. The clustering of peptide MD simulations revealed four stable conformations of *FAM*-Y_4R_4 (Fig. S4†), randomly distributed in two separate boxes. Two independent MD simulations, named MD I and MD II, were conducted for a duration of 100 ns each. The radius of gyration (R_g) value, which represents the average root mean square distance of all atoms from the center of mass of the peptide, was used to assess structural compactness. In both MD I and II trajectories, the R_g values decreased from approximately 20 to 13 Å (Fig. S5A†), indicating a more compact structure. The solvent-accessible surface area (SASA) value, which quantifies the surface area of the peptide interacting with solvent molecules, also decreased throughout MD I and II, further supporting the compactness and aggregation of the peptides (Fig. S5B†). Additionally, the aggregation process was associated with an increase in hydrogen bonding. The number of hydrogen bonds formed between and across all peptides increased during the MD I and II simulations (Fig. S5C†). To visualize the aggregation process during the production MD simulations, representative systems at 25, 50, 75, and 100 ns were depicted (Fig. S5D†). These snapshots provide insight into the kinetics of aggregation for the four *FAM*-Y_4R_4 peptides over the course of the 100 ns simulations. Notably, MD II exhibited faster aggregation kinetics, as evidenced by a more rapid decrease in R_g and SASA values, as well as a quicker increase in the number of hydrogen bonds.

The clustering of MD I and II trajectories depicted two more stable clusters for the aggregated form of *FAM*-Y_4R_4. The aggregated structure at 100 ns of MD I and II which are belonged to the most stable clusters and the details of their interactions are shown in Fig. 3 and S6.†

The distance map represents the distance between all possible amino acid residue pairs of a biomolecule in the 3D structure. The distance map of these aggregated peptides showed short distances between some residues of these peptides (Fig. 3B and S6B†). The hydrogen bonds and hydrophobic contacts (carbon atoms in contact with other carbon atoms) as important non-covalent interactions and aggregation driving forces were detected between all pairs of amino acids (Fig. 3C and S6C†). More importantly, some other non-covalent interactions such as cation–π and π–π are detected in this aggregated form of *FAM*-Y_4R_4 (Fig. 3D).

A cation–π interaction is defined between a cationic side chain of either lysine or arginine and an aromatic side chain with a distance of less than 6 Å.[25] The cation–π interactions were detected between R–Y and R–*FAM* in these aggregated structures which was confirmed by our experimental results (Fig. 2 and S3†). The π–π interactions occur between two aromatic rings with a distance and angle of less than 6.0 Å and 30°, respectively.[26] The π–π interactions were detected between Y–Y, Y–*FAM*, and *FAM*–*FAM* in these aggregated structures. All of these interactions stabilized the aggregates.

Peptides lack well-defined secondary structures, which necessitates a structural ensemble to describe their structure and function. During the aggregation process, the peptides undergo conformational motions and come close to each other, which causes the formation and breaking of some non-covalent interactions to reach a stable aggregated form. Aggregation is

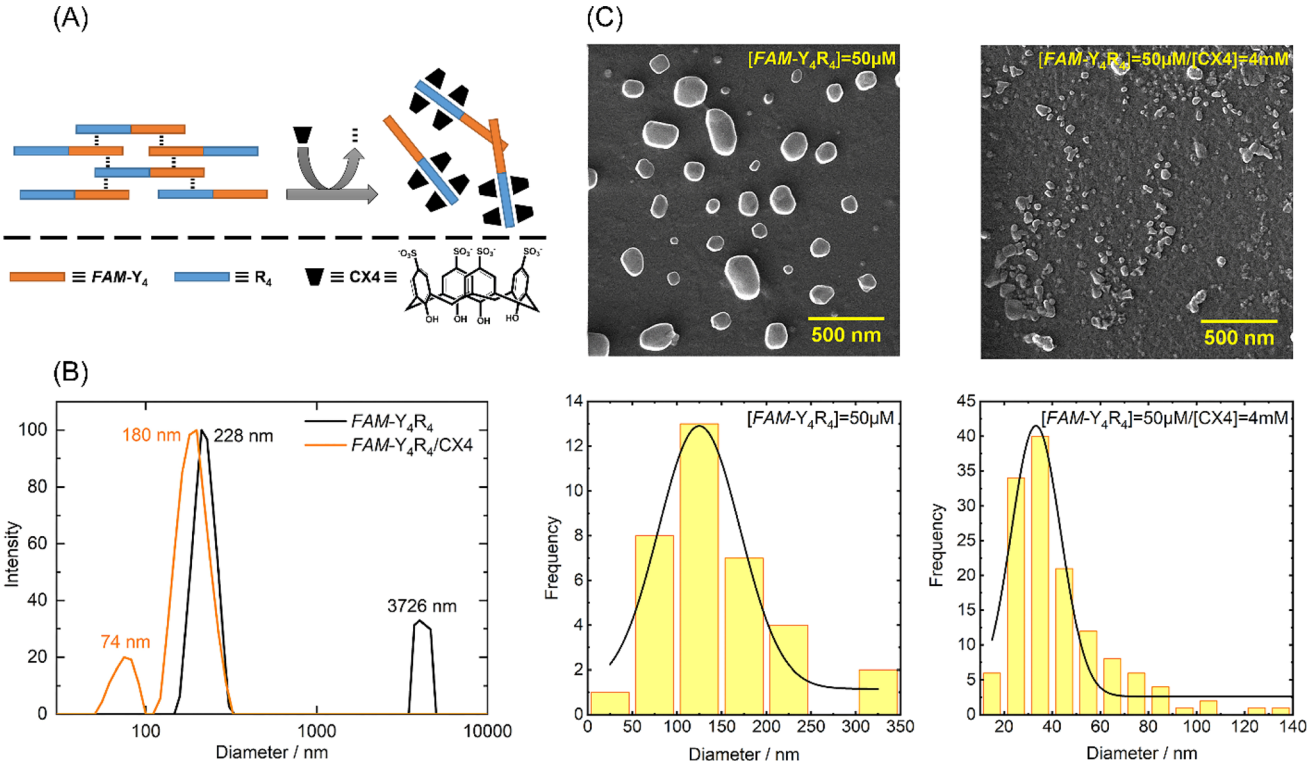

Fig. 2 (A) Schematic illustration of the cation–π and π–π interactions that drive peptide aggregation. Subsequently, the addition of CX4 triggers the breakdown of these aggregates. (B) Size distribution of particles in a solution containing either the peptide or peptide/CX4 measured by dynamic light scattering (DLS). (C) FE-SEM images depicting the morphology of the peptide and the peptide/CX4 aggregates, along with their respective size distributions.

a complex phenomenon with different influencing factors, of which amino acid sequence is one of the most important.[27,28]

Tyrosine is a hydrophobic amino acid with an aromatic side chain. On the other hand, arginine is a positively charged amino acid with a guanidino group, resulting in a cation. *FAM* contains both aromatic and hydrophilic parts. Here, the most two stable clusters were detected for aggregated structures. The peptide aggregated structures are stabilized with different non-covalent interactions explained above. Conventional hydrogen bonds are the dominant interactions for stabilizing aggregated structures.[29] But in these aggregated structures more stabilization and ordering were offered with packing interactions between two aromatic rings (π–π) and the side chain of arginine and aromatic rings (cation–π). A wide range of roles in proteins has been identified for interactions involving the π electron cloud of aromatic rings. Cation–π and π–π interactions were highlighted in the stability of peptide and protein structures,[25,30,31] and supramolecular assemblies.[32–34] The cation–π interaction is essential in the formation of the aggregate because in the absence of the cation–π interactions, the π–π interactions would lead to the formation of micelles or liposomes.

Cellular uptake

The uptake of the peptide with MCF-7 and A549 cells was investigated using flowcytometry and fluorescence imaging. Flowcytometry was utilized to quantify the amount of the peptide inside the live cells in terms of MFI values, as a function of the peptide and CX4 concentration. The recorded MFI values in Fig. 4 demonstrate that both *FAM*-Y_4R_4 and *FAM*-Y_4R_4/CX4 were uptake by the cells after 18 hours of incubation. The maximum cellular uptake of *FAM*-Y_4R_4 occurs at a concentration of 100 nM. However, as the concentration increases, the cellular uptake decreases due to peptide aggregation. It is important to note that peptide aggregation is a concentration-dependent phenomenon,[27,35] and very often the cellular uptake of peptide aggregates is lower compared to individual peptide molecules. The solubilization of *FAM*-Y_4R_4 peptides with CX4 has been observed to enhance the internalization. Notably, *FAM*-Y_4R_4/CX4 exhibits the most efficient cell uptake at concentrations equal to or greater than 900 nM of the peptide in the presence of 4 mM of CX4. Previous studies have also shown that CX4 can enhance the cell uptake of LCG, acting as its host fluorescent dye.[19] A549 cells demonstrate higher uptake compared to MCF7 cells. Repotente Jr *et al.* have also reported higher cellular uptake of gold nanoparticles with A549 cells compared to MCF7 cells.[36] This higher uptake in A549 cells may be attributed to their alveolar origin tissue.

Endocytosis and diffusion (direct penetration) are the main cellular uptake mechanisms. The diffusion across the cell membrane is faster than endocytosis. Eighteen hours was a plentiful time for the cells to endocytose the peptide. To favor diffusion, the peptide incubation time was shortened to one

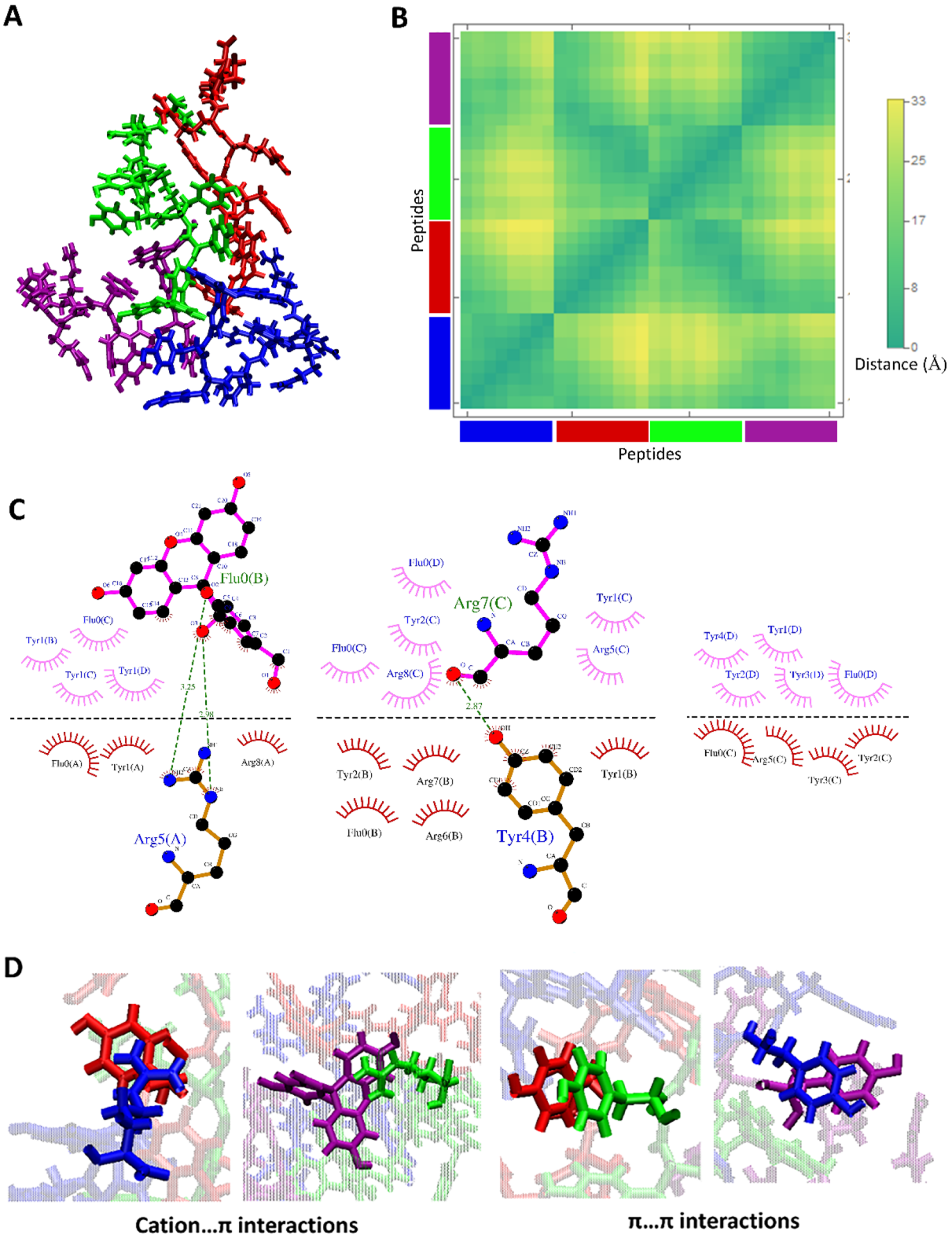

Fig. 3 (A) The representation of the MD II system at 100 ns. (B) The distance map of the four *FAM*-Y_4R_4 peptides in the structure of panel A. (C) The hydrogen bonds, and hydrophobic contacts between four *FAM*-Y_4R_4 peptides in the structure of panel A, and (D) some examples of other non-covalent interactions such as cation–π and π–π.

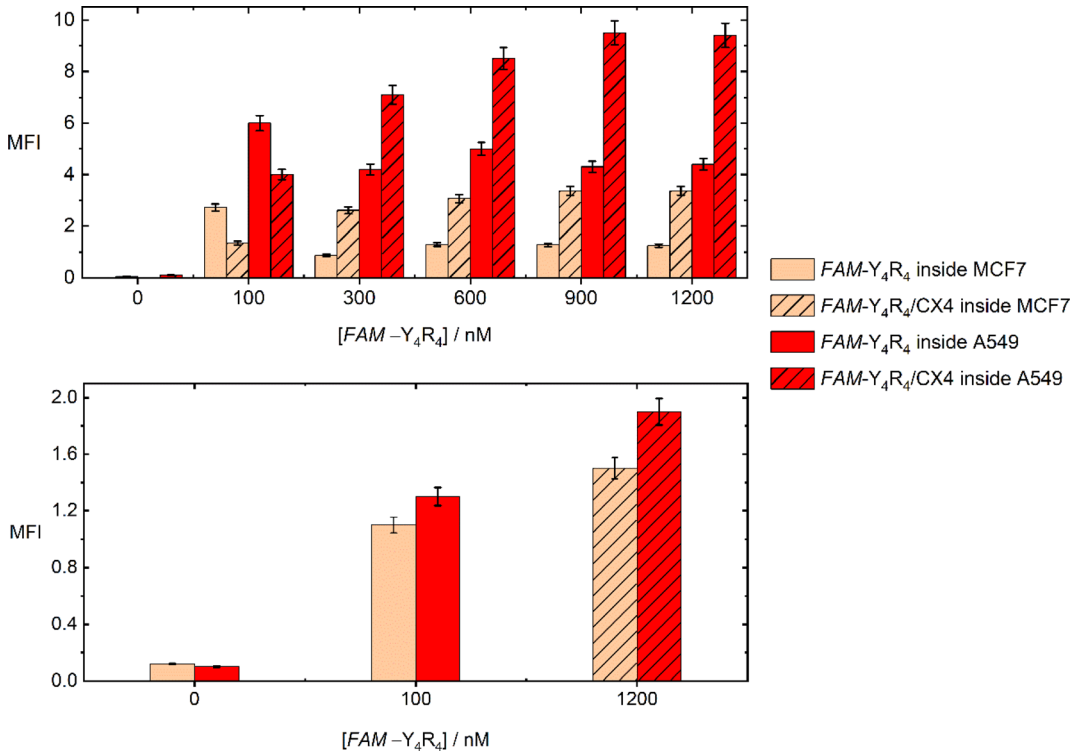

Fig. 4 Mean fluorescence intensity (MFI) values of MCF7 and A549 cells incubated with varying concentrations of *FAM*-Y_4R_4, with and without 4 mM of CX4, were measured after 18 hours (top) and 1 hour (bottom) of incubation.

hour, and the MFI was remeasured (Fig. 4). The most effective concentration of *FAM*-Y_4R_4 (100 nM) and *FAM*-Y_4R_4/CX4 (1200 nM/4 mM) – in which the maximum MFI values were obtained after 18 hours – was applied. The result showed that the peptide in the presence and absence of CX4 diffused to the cells; however, compared to the 18 hours experiment, a lower amount of peptide molecules was found inside the live cells. The more internalized peptide molecules after 18 hours of incubation indicates that endocytosis is more efficient than diffusion in peptide uptake. After 1 h incubation, the MFI of peptide in the presence of CX4 is fairly higher than the peptide alone which means that CX4 has slightly facilitated the diffusion.[37] Decorating the hydroxyl group of CX4 with alkyl chains and incubating with octaarginine has been shown to increase the octaarginine cell entry *via* diffusion.[6] Our results indicates that CX4 alone – even in the absence of CX4 alkylation – paves the way for diffusion. Nevertheless, endocytosis remains the main uptake pathway, as the MFI values of *FAM*-Y_4R_4/CX4 are almost five times higher after 18 hours of incubation.

In order to further validate the uptake and intracellular distributions of the peptide, the cells were treated with *FAM*-Y_4R_4 or *FAM*-Y_4R_4/CX4 and subjected to fluorescence microscopy (Fig. S8†) and CLSM (Fig. 5). *FAM*-Y_4R_4, with and without CX4, was abundantly observed in the cytoplasm of the cells. *FAM*-Y_4R_4 is observable in the nucleus of some MCF7 and A549 cells (distinguished with the white arrows).

A similar observation has been reported for some amphipathic CPPs such as Pep-1 (KETWWETWWTEWSQPKKKRKV). Its cationic domain (KKKRKV) can facilitate the transportation of the peptide into the cell nucleus through nuclear pores. This cationic domain is referred to as the nuclear localization signal (NLS).[38] Pep-1 consists of a tryptophan-rich, hydrophobic domain fused to an NLS domain. Despite their differences in length, both *FAM*-Y_4R_4 and Pep-1 are amphipathic in nature, composed of an aromatic-rich, hydrophobic domain fused to a cationic domain that functions as an NLS. Detailed explanation of the mechanism behind the direct penetration of guanidinium-rich molecules has been given in the literature.[7,39] The guanidino group of the arginine side chains drives the internalization of arginine-rich CPPs, including *FAM*-Y_4R_4, by creating pores in the cell membrane and inducing membrane multilamellarity.

Supramolecular bindings of curcumin and CX4 to *FAM*-Y_4R_4

CPPs bind to their cargo either covalently or non-covalently (supramolecularly). Covalently conjugating the CPP with its cargo carries the risk of potentially altering the biological activity of the cargo. Conversely, non-covalent binding allows for reversible association between the cargo and CPP, enabling the cargo to dissociate from the CPP intact. The CPP/cargo supramolecular complex is able to traverse the cell membrane, and upon reaching the cytosolic side, the CPP dissociates from its cargo and undergoes proteolysis by cytosolic proteases; therefore, re-association with its cargo is not possible. An additional advantage of this method is that the CPP provides protection to its cargo, thereby increasing its serum half-life.[40]

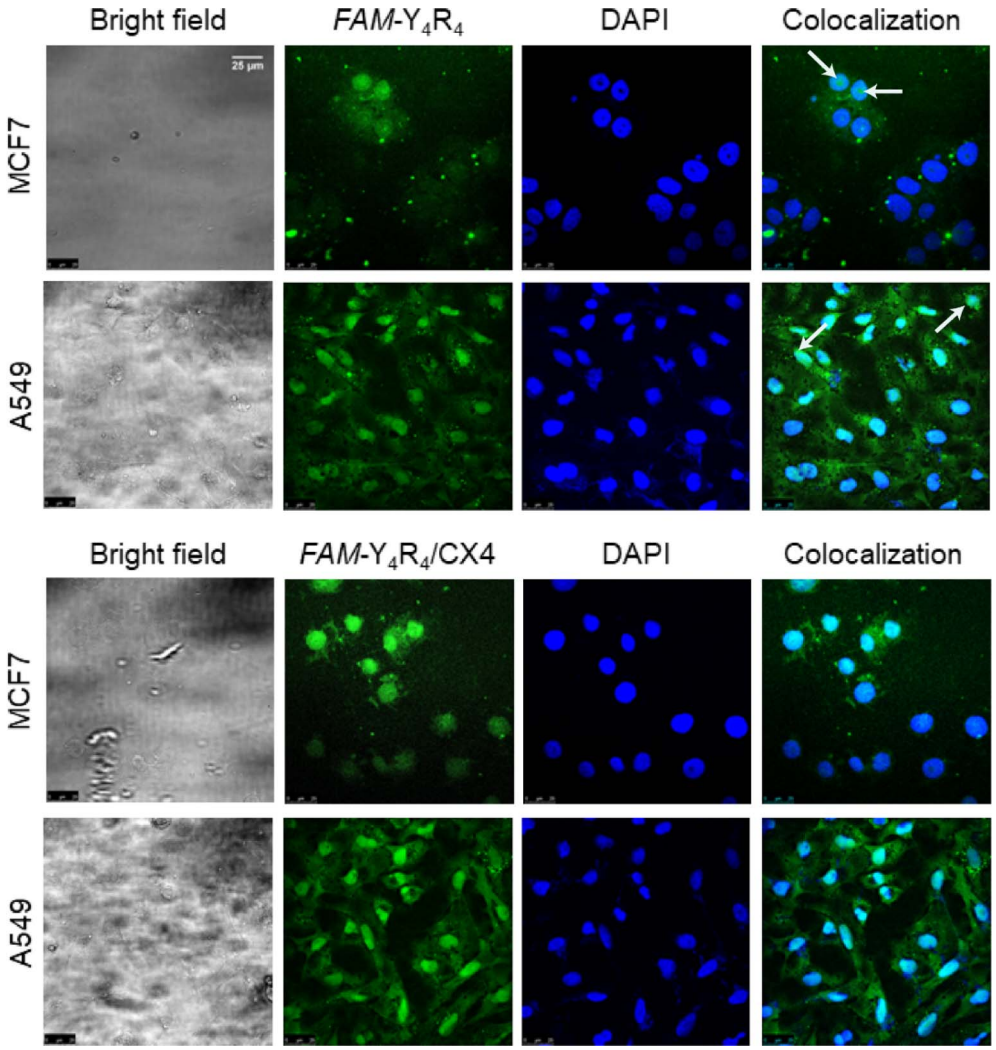

Fig. 5 Confocal microscopy images of MCF7 and A549 cells. The cells were incubated with *FAM*-Y_4R_4 (100 nM) or *FAM*-Y_4R_4/CX4 (50 μM/1 mM) at 37 °C for 18 hours. Cell nuclei stained with DAPI dye are represented in blue, while the peptides are represented in green. The white arrows distinguish the peptide inside the nuclei.

Curcumin contains aromatic chemical groups that can interact with the sidechains of Y_4 through a process known as π-stacking (Fig. 6A). This interaction is characterized by a decrease in the fluorescence intensity of tyrosine and an increase in the molar absorption of curcumin. We utilized these spectral properties to outline the binding isotherms. To exclude the nonspecific binding between the side chains of Y_4 and R_4 we used tyrosine in the form of free amino acid instead of *FAM*-Y_4R_4 for fluorescence titration with curcumin (Fig. 6B).

We double demonstrate the binding of curcumin to the tyrosine side chain using a UV-vis spectrometer (Fig. 6C). We opted to use phenol instead of *FAM*-Y_4R_4 as a representative of the tyrosine sidechain during the spectral titration. Because our primary focus was to investigate the π-stacking interaction between the aromatic portion of Y_4 and curcumin. The presence of *FAM* and R_4 in the spectral titration could potentially complicate the results by influencing the molar absorption of curcumin.

We employed a 1 : 1 model (one host to one guest) in a nonlinear regression algorithm[28] to calculate the binding constants. The K_a values obtained from fluorescence and UV-vis titration were found to be 1.6×10^5 M^{-1} and 4.6×10^6 M^{-1} respectively. Taking the average of these two values, the overall binding constant was determined to be $K_a = 2.38 \times 10^6$ M^{-1}. The ability of Y_4 to bind strongly to curcumin is a promising indication for considering our peptide for transporting other PWSDs into live cells.

Curcumin is widely recognized as an insoluble molecule, with a solubility of 30 nM (11 ng mL^{-1}) in water.[41] However, when bound to the tyrosines of *FAM*-Y_4R_4, the solubility of curcumin enormously increased to 400 nM. To assess the solubility of curcumin in the presence and absence of the peptide, we measured its absorption peak at 425 nm and extrapolated the concentrations from the curcumin standard curve.

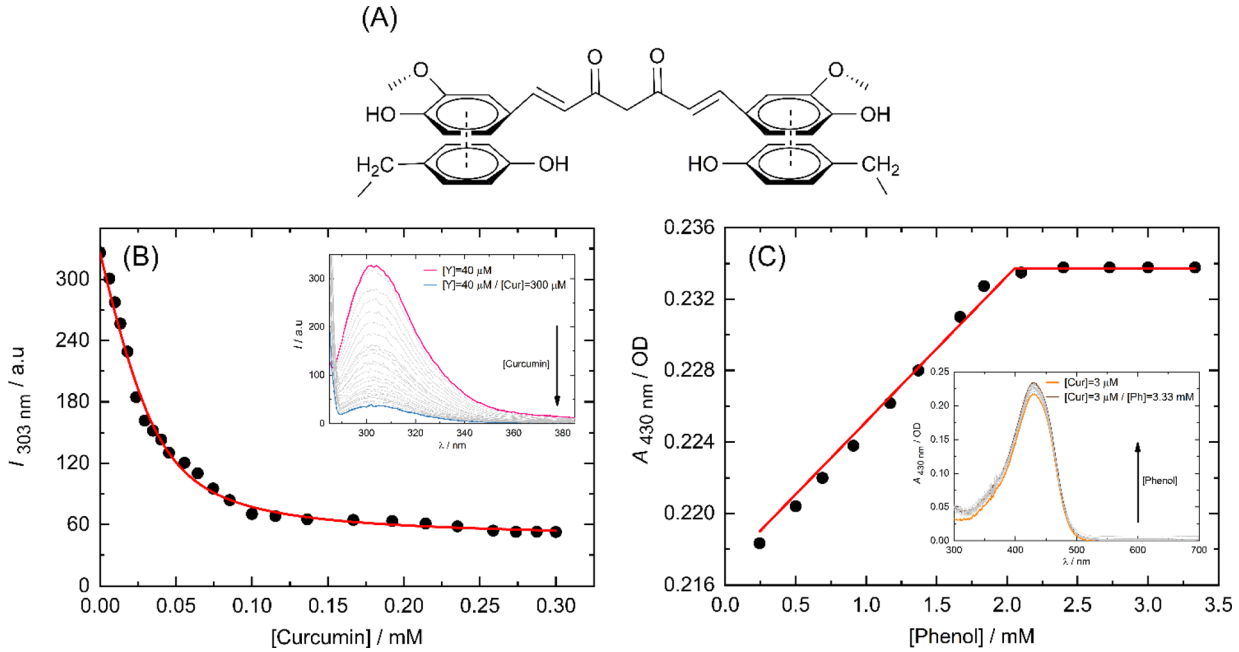

Fig. 6 Schematic representation of π-stacking interactions between two tyrosine side chains and a curcumin molecule (A). The binding isotherms of curcumin (Cur) to tyrosine (Y) and phenol (Ph) were depicted in B and C respectively which were obtained through fluorescence and UV-vis spectral titration, respectively. The insets show the spectral titrations.

Arginine side chain enters the cavity of CX4. The average binding strength of CX4 molecules to arginine side chains of *FAM*-Y_4R_4 was measured with IDA method. The obtained binding strength is K_a (CX4/R_4) = 4.5×10^5 M^{-1} (Fig. S7†). CX4 can weakly bind to *FAM* with K_a (CX4/*FAM*) = 3.9×10^4 M^{-1}.[42]

Cell viability and toxicity assays

To evaluate the toxicity of various samples including the peptide, curcumin, the peptide/curcumin, the peptide/CX4, the (peptide/curcumin)/CX4 and CX4 on the cells, MTT viability test was conducted (Fig. 7). The cells were treated with different concentrations of the aforementioned samples for 18 hours. The results indicated that at its highest concentration, *FAM*-Y_4R_4 caused a maximum decrease in MCF-7 cell viability of 20%. However, when combined with CX4 (*FAM*-Y_4R_4/CX4), the cell viability decreased by 40%. This finding suggests that CX4 drives more peptides into the cells. In the mixture of *FAM*-Y_4R_4 and CX4, the concentration of CX4 was fixed at 4 mM, which was significantly higher than the concentration of the peptide in the micromolar range. This ensured an excess of CX4

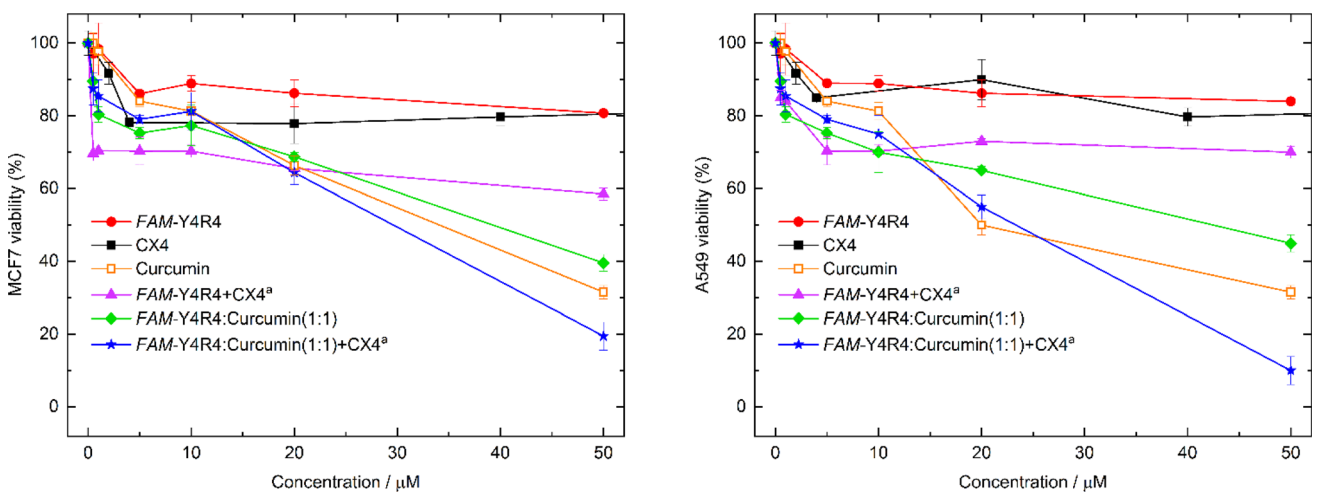

Fig. 7 Viability of MCF-7 cells (left) and A549 cells (right) after incubation with various concentrations of *FAM*-Y_4R_4, curcumin, CX4, *FAM*-Y_4R_4/curcumin, *FAM*-Y_4R_4/CX4, or (*FAM*-Y_4R_4/curcumin)/CX4[a]. The concentration of CX4 was maintained at a maximum of 4 mM in *FAM*-Y_4R_4/CX4 and (*FAM*-Y_4R_4/curcumin)/CX4 complexes.

molecules (by 80 times) to ensure accessibility to every arginine's side chain. CX4, even up to 200 μM, did not significantly reduce the toxicity of MCF7 and A549 cells beyond 22% (results not shown in the graph). *In vivo* studies have demonstrated that CX4 exhibits no hemolytic toxicity at concentrations up to 5 mM and does not induce non-specific immunological reactions.[43]

Curcumin exhibits cytotoxicity in a manner that is dependent on the dosage administered. Notably, the *FAM*-Y_4R_4/curcumin and the (*FAM*-Y_4R_4/curcumin)/CX4 complexes demonstrated a more pronounced dose-dependent suppression of cell growth compared to curcumin alone. To validate these findings, we conducted the toxicity experiment on A549 cells. The results obtained for *FAM*-Y_4R_4 and CX4 were consistent with those observed in the MCF7 cells. However, the peptide/CX4 complex exhibited higher toxicity in MCF7 cells. Conversely, curcumin and peptide/curcumin showed equal toxicity in both cell lines, while the (*FAM*-Y_4R_4/curcumin)/CX4 complex displayed greater toxicity in A549 cells compared to MCF7 cells. This discrepancy can be attributed to the increased uptake of the peptide/CX4 complex by A549 cells discussed earlier (Fig. 4), resulting in a higher uptake of the toxic cargo (curcumin) when complexed with the cell-penetrating peptide (CPP).

Various carriers for curcumin, including nanoparticles, hydrogels, nanostructures, liposomes, polymeric micelles, quantum dots, and polymeric blend films have been documented.[44] In a recent study, a cyclic peptide was synthesized and utilized as a carrier for curcumin and doxorubicin. Both covalent and supramolecular modifications were employed to bind curcumin with the peptide. The covalent modification of curcumin resulted in reduced toxicity towards LLCPK, SKOV-3, and CCRF-CEM cell lines. On the other hand, in consistency to our toxicity results; the supramolecular binding of curcumin/doxorubicin to the peptide exhibited enhanced efficacy in killing cancer cells.[45]

Ratrey *et al.* used an octaarginine CPP (R_8) to bind to curcumin *via* cation–π interactions. The resulting complex of R_8/curcumin exhibited enhanced antibacterial and anticancer activity compared to curcumin alone.[41] However, directly engaging the cargo with the sidechain of R_8 may hinder its direct penetration across the cell membrane.[7] In contrast, our peptide utilizes Y_4, which exhibits a stronger affinity for curcumin or any other PWSD (peptide-wrapped small drug), enabling the R_4 portion to bind to CX4 and fulfill its role in cellular penetration.

Conclusion

FAM-Y_4R_4/CX4 complex represents a novel amphipathic CPP with promising potential. This complex consists of a binding component (Y_4) that hosts PWSDs, and a cell-penetrating component (R_4/CX4) that facilitates the entry of the peptide into live cells. The shorter length of R_4 in this peptide offers an advantage, as it allows for more efficient synthesis compared to conventional oligoarginine-based CPPs, which typically contain 7 to 9 arginine residues. Additionally, CPP aggregation often leads to reduced effectiveness, but the presence of CX4 in our complex prevents the side chains of R_4 from forming cation–π interaction with the Y_4 sidechain that avoids aggregation and enhances cell uptake. Importantly, our CPP complex significantly improves the solubility of curcumin and effectively delivers it into live cells, thereby enhancing curcumin's anticancer properties.

Data availability

All data generated and/or analyzed during this study are included in this published article or its ESI.†

Author contributions

ZA conducted the toxicity assays on A549 cells. NS performed the molecular dynamics simulations. MH carried out the remaining experiments. RZ, WN, and KK provided scientific guidance as advisors. AN supervised the project and prepared the manuscript.

Conflicts of interest

There are no conflicts to declare.

Acknowledgements

The authors thank the Iran National Science Foundation for financing this work with Grant No. 96009524. We also thank the National Institute of Genetic Engineering and Biotechnology (NIGEB) for its support.

References

1 A. Komin, L. Russell, K. Hristova and P. Searson, *Adv. Drug Delivery Rev.*, 2017, **110**, 52–64.
2 A. F. Schneider, M. Kithil, M. C. Cardoso, M. Lehmann and C. P. Hackenberger, *Nat. Chem.*, 2021, **13**, 530–539.
3 J. D. Ramsey and N. H. Flynn, *Pharmacol. Ther.*, 2015, **154**, 78–86.
4 J. Xie, Y. Bi, H. Zhang, S. Dong, L. Teng, R. J. Lee and Z. Yang, *Front. Pharmacol*, 2020, **11**, 697.
5 J. B. Rothbard, E. Kreider, C. L. VanDeusen, L. Wright, B. L. Wylie and P. A. Wender, *J. Med. Chem.*, 2002, **45**, 3612–3618.
6 C. Huang, Y. C. Liu, H. Oh, D. S. Guo, W. M. Nau and A. Hennig, *Chem.–Eur. J.*, 2024, **30**, e202400174.
7 H. D. Herce, A. E. Garcia and M. C. Cardoso, *J. Am. Chem. Soc.*, 2014, **136**, 17459–17467.
8 Z. Vaezi, A. Bortolotti, V. Luca, G. Perilli, M. L. Mangoni, R. Khosravi-Far, S. Bobone and L. Stella, *Biochim. Biophys. Acta, Biomembr.*, 2020, **1862**, 183107.
9 W. P. R. Verdurmen, R. Wallbrecher, S. Schmidt, J. Eilander, P. Bovee-Geurts, S. Fanghänel, J. Bürck, P. Wadhwani, A. S. Ulrich and R. Brock, *J. Controlled Release*, 2013, **170**, 83–91.
10 L. Vasconcelos, T. Lehto, F. Madani, V. Radoi, M. Hällbrink, V. Vukojević and Ü. Langel, *Biochim. Biophys. Acta, Biomembr.*, 2018, **1860**, 491–504.

11 L. Baldini, A. Casnati, F. Sansone and R. Ungaro, *Chem. Soc. Rev.*, 2007, **36**, 254–266.
12 A. D'Urso, G. Brancatelli, N. Hickey, E. Farnetti, R. De Zorzi, C. Bonaccorso, R. Purrello and S. Geremia, *Supramol. Chem.*, 2016, **28**, 499–505.
13 M. Selkti, A. W. Coleman, I. Nicolis, N. Douteau-Guével, F. Villain, A. Tomas and C. de Rango, *Chem. Commun.*, 2000, 161–162.
14 A. Lazar, E. Da Silva, A. Navaza, C. Barbey and A. W. Coleman, *Chem. Commun.*, 2004, 2162–2163.
15 M. R. Islam, A. Rauf, S. Akash, S. I. Trisha, A. H. Nasim, M. Akter, P. S. Dhar, H. A. Ogaly, H. A. Hemeg, P. Wilairatana and M. Thiruvengadam, *Biomed. Pharmacother.*, 2024, **170**, 116034.
16 M. Shahabi, R. Hajihosseini, W. M. Nau, K. A. Noghabi and A. Norouzy, *Int. J. Pept. Res. Ther.*, 2020, **26**, 2633–2640.
17 A. Norouzy, A. I. Lazar, M. H. Karimi-Jafari, R. Firouzi and W. M. Nau, *Amino Acids*, 2022, 1–11.
18 P. Fattahi, N. Salehi, J. Mohammadi, A. Norouzy and S. M. Moazzeni, *J. Pept. Sci.*, 2023, **29**, e3480.
19 A. Norouzy, Z. Azizi and W. M. Nau, *Angew. Chem., Int. Ed.*, 2015, **54**, 792–795.
20 E. Vivès, P. Brodin and B. Lebleu, *J. Biol. Chem.*, 1997, **272**, 16010–16017.
21 J. Park, J. Ryu, K.-A. Kim, H. J. Lee, J. H. Bahn, K. Han, E. Y. Choi, K. S. Lee, H. Y. Kwon and S. Y. Choi, *J. Gen. Virol.*, 2002, **83**, 1173–1181.
22 G. Tünnemann, G. Ter-Avetisyan, R. M. Martin, M. Stöckl, A. Herrmann and M. C. Cardoso, *J. Pept. Sci.*, 2008, **14**, 469–476.
23 A. Rodger, in *Encyclopedia of Biophysics*, ed. G. Roberts and A. Watts, Springer Berlin Heidelberg, Berlin, Heidelberg, 2018, pp. 1–6, DOI: 10.1007/978-3-642-35943-9_634-1.
24 D. A. Dougherty, *Acc. Chem. Res.*, 2013, **46**, 885–893.
25 J. P. Gallivan and D. A. Dougherty, *Proc. Natl. Acad. Sci. U. S. A.*, 1999, **96**, 9459–9464.
26 A. Jain and R. Sankararamakrishnan, *J. Chem. Inf. Model.*, 2011, **51**, 3208–3216.
27 K. L. Zapadka, F. J. Becher, A. Gomes dos Santos and S. E. Jackson, *Interface Focus*, 2017, **7**, 20170030.
28 A. Norouzy, A. I. Lazar, M. H. Karimi-Jafari, R. Firouzi and W. M. Nau, *Amino Acids*, 2022, **54**, 277–287.
29 M. Meli, G. Morra and G. Colombo, *Biophys. J.*, 2008, **94**, 4414–4426.
30 N. Queralt-Rosinach and J. Mestres, *Eur. Biophys. J.*, 2010, **39**, 1471–1475.
31 M. L. Waters, *Biopolymers*, 2004, **76**, 435–445.
32 S. A. Vuai, M. G. Sahini, I. Onoka, L. W. Kiruri and D. M. Shadrack, *RSC Adv.*, 2021, **11**, 33136–33147.
33 A. Norouzy, M. Habibi-Rezaei, D. Qujeq, M. Vatani and A. Badiei, *Bull. Korean Chem. Soc.*, 2010, **31**, 157.
34 A. Norouzy, D. Qujeq and M. Habibi-Rezaei, *React. Kinet. Catal. Lett.*, 2009, **98**, 391–401.
35 S.-j. Choi, W.-j. Jeong, S.-K. Kang, M. Lee, E. Kim, D. Y. Ryu and Y.-b. Lim, *Biomacromolecules*, 2012, **13**, 1991–1995.
36 E. C. Repotente Jr, A. J. Carreon, M. K. Devanadera, M. S. Esmalla and M. Santiago-Bautista, *Front. Mater.*, 2022, **9**, 933749.
37 R. Lalor, H. Baillie-Johnson, C. Redshaw, S. E. Matthews and A. Mueller, *J. Am. Chem. Soc.*, 2008, **130**, 2892–2893.
38 G. Guidotti, L. Brambilla and D. Rossi, *Trends Pharmacol. Sci.*, 2017, **38**, 406–424.
39 C. Allolio, A. Magarkar, P. Jurkiewicz, K. Baxová, M. Javanainen, P. E. Mason, R. Šachl, M. Cebecauer, M. Hof and D. Horinek, *Proc. Natl. Acad. Sci. U. S. A.*, 2018, **115**, 11923–11928.
40 J. Regberg, A. Srimanee and Ü. Langel, *Pharmaceuticals*, 2012, **5**, 991–1007.
41 P. Ratrey, S. V. Dalvi and A. Mishra, *ACS Omega*, 2020, **5**, 19004–19013.
42 S. Gawhale, Y. Thakare, D. Malkhede and G. J. O. Chaudhari, *Opt. Photonics J.*, 2014, **4**, 237.
43 D.-S. Guo and Y. Liu, *Acc. Chem. Res.*, 2014, **47**, 1925–1934.
44 S. Sharifi, N. Fathi, M. Y. Memar, S. M. Hosseiniyan Khatibi, R. Khalilov, R. Negahdari, S. Zununi Vahed and S. Maleki Dizaj, *Phytother. Res.*, 2020, **34**, 1926–1946.
45 S. Darwish, S. Mozaffari, K. Parang and R. Tiwari, *Tetrahedron Lett.*, 2017, **58**, 4617–4622.